Hats and pancakes in the sky: high-speed droplet dynamics

K. Pentland,[1, a)] R. Cimpeanu,[2] and E. Brambley[2, 3]
[1)] *EPSRC & MRC Centre for Doctoral Training in Mathematics for Real-World Systems, University of Warwick*
[2)] *Mathematics Institute, Zeeman Building, University of Warwick*
[3)] *Warwick Manufacturing Group, University of Warwick*

(Dated: 11 September 2020)

Accurately modelling water droplets that impinge on the surface of flying aircraft and subsequently freeze (damaging critical flight components) presents a significant challenge in the aviation industry. The large air velocities specific to the movement of aircraft are sufficient to influence a droplet's trajectory, as well as its shape and possible break-up. In this report, potential improvements to the assumptions and approximations made in an existing theoretical droplet trajectory and deformation model are suggested. Sensitivity analysis identifies weakly influencing model parameters (i.e. gravity, vertical velocity and viscosity) and reveals the extent to which others (i.e. background flow, forces and experimental coefficients) drive the model and/or limit its predictive capability. An alternative numerical model is detailed, coupling local flow around the droplet with the simulated (or analytically approximated) global flow of an incoming aerofoil. High resolution direct numerical simulations (DNS) are deployed to solve the two-phase Navier-Stokes equations. Interfacial deformation, flow velocities and pressure profiles are determined and are used to better inform and validate the existing model. Conditions neglecting vertical displacement and methods for approximating the background flow are verified, however the droplet is found to only deform as an oblate spheroid (without oscillating) for a very short time period before exhibiting more localised and one-sided deformation on its face. This initial modelling approach illustrates the future potential of using DNS as a self-contained method for simulating changes in droplet morphology in challenging flow regimes, using state-of-the-art computational resources in an efficient manner.

I. INTRODUCTION

The study of fluid droplets that evolve within a secondary fluid phase (e.g. water droplets in air) can be roughly split into two main areas of focus: pre-impact and post-impact dynamics. Pre-impact dynamics involve studying a droplet's trajectory, deformation and, if certain conditions are met, its subsequent breakup. Post-impact dynamics consider the spreading, sticking and splashing of a droplet (or smaller secondary droplets after breakup) following contact with a solid or liquid surface.

Investigations into both areas have proven highly challenging yet are far-reaching, not just within fluid mechanics but to a variety of phenomena in industrial design and manufacturing processes. Droplet experiments and computational modelling have been key in establishing the next generation of ink-jet[1] and 3D printers, whilst the development of spray technologies have contributed to improved efficiency in combustion engines, materials coating, cooling systems and agricultural crop spraying[2]. Medical applications include bloodstain pattern analysis in the forensic sciences[3], fabrication techniques for efficient drug delivery and modelling virus transmission via airborne saliva droplets[4].

Of particular interest however are aeronautical applications in which aircraft travel through naturally suspended water droplets (clouds) of varying size and distribution at high velocity. Droplets can impinge upon the surface of the aircraft, subsequently collecting and freezing on the wings, engine intake and other critical flight components. This reduces aerodynamic efficiency and in the worst cases can lead to aircraft failure. Extensive reviews have been carried out on the adverse effects of rainfall and icing on aircraft performance as well as on methods of in-flight icing detection[5–7]. To accurately model and predict under what conditions these adverse effects occur, it is of particular importance to study the pre-impact dynamics of droplet deformation and breakup in the close vicinity of an approaching aerofoil (wing-shaped geometry). While this report focuses on droplets prior to impact, post-impact dynamics following impingement are also critical to understanding the effects of sticking, splashing and retention of water on aircraft surfaces (see two excellent reviews of impact dynamics[8,9]).

Modelling secondary atomisation (droplet breakup) analytically is very challenging due to the, often violent and seemingly chaotic, topological changes that arise on the droplet interface as it disintegrates[10]. Many attempts have however been made to analytically model the overall shape deformation of an initially spherical droplet by placing it in unidirectional flow. The droplet is then assumed to deform into an ellipsoidal shape (oblate spheroidal in 3D) under the effects of the incoming airflow, thus neglecting the details of local deformations on the droplet surface.

One of the first studies was the Taylor analogy breakup (TAB) model[11] that approximated the equatorial displacement of an oscillating (deforming) droplet by a classical harmonic mass-spring system. This analogy was originally made by Taylor[12], who discusses the balance of forces, set up by flow around the droplet, acting to deform and restore its shape. Pressure forces set up by inertial effects of the air act to deform the droplet whereas both interfacial surface tension and viscous forces act to restore it. Once restoring forces are overcome by inertia, the droplet undergoes a specific type of breakup not captured by the model (refer to Fig. 1).

Improved investigations followed, one being Clark's lin-

[a)] Electronic mail: kamran.pentland@warwick.ac.uk

earised semi-analytical model[13] (prohibiting large deformations) in which forces are balanced around the axisymmetric 'half-droplet' centre of mass instead of the equator. The droplet deformation and breakup (DDB) model was introduced by Ibrahim et al.[14] in which forces are balanced by changes in kinetic and potential energy. Droplet volume instead of area was chosen as a conserved quantity, greatly affecting individual force contributions. Ibrahim et al. compare all three models to early experimental work[15] of droplets exposed to airflow in a wind tunnel. It was found that earlier models overestimated the magnitude of deformation, however analysis was limited to only one case study.

More recently, a droplet ratio deformation (DRD) model[16] was formulated and improved by calculating more accurate surface area changes and introducing (time-dependent) slip velocities close to the droplet. Although the DRD model matched (newer) experiments well, previous models (TAB/Clark/DDB) again over- or underestimated droplet deformation. Whereas the previous models studied droplets exposed to a *constant* background flow, the slip velocities in the DRD model could account for an *accelerating* flow field, just like the one created by an approaching aerofoil. Building on this, the same authors develop an extension to the DRD model in which they couple deformation with the spatial trajectory of the droplet[17]. This model is calibrated and verified using excellent experimental rotating arm facilities[18] and is discussed at length in Section II.

Much experimental effort has gone into trying to image complex droplet geometries following the onset of breakup under differing flow conditions. The type of breakup a droplet experiences has a profound impact on the subsequent atomisation process. Many different modes of breakup with varying descriptive names have been observed over the years however they are can be broadly categorised into five main groups[19]: vibrational, bag, multi-mode, sheet-thinning and catastrophic (see Fig. 1). Although out of the scope of the present report, droplet breakup is an important and challenging area of pre-impact dynamics and a brief introduction is helpful to provide an overall picture of the field.

The review by Theofanous[20] categorises these modes (regimes) into two broader classes of breakup: Rayleigh-Taylor piercing (RTP) and shear-induced entrainment (SIE). He states the RTP regime as one "governed by the Rayleigh-Taylor instability; a flattened drop penetrated by one or more unstable waves" (bag and multi-mode) and the SIE regime as one "involving a peeling action that results from a combination of Kelvin-Helmholtz instabilities, mean motion due to viscous shearing, and local capillary breakups of films and filament" (sheet-thinning and catastrophic). Much pre-impact study has been focused on categorising these regimes in terms of various dimensionless groupings, however the differing flow conditions (sub- and supersonic flows) and experiments used (shock tubes, drop towers etc.) have lead to varying, sometimes contradictory, results.

In the last two decades, efficient direct numerical simulations (DNS) have been developed that utilise state-of-the-art Volume-of-Fluid and adaptive meshing techniques[21] in order to solve the multi-phase equations of fluid motion. Combined with the use of high performance computing facilities, highly accurate simulations can be produced on timescales up to $\mathscr{O}(10^3)$ CPU hours, enabling multi-phase flow to be visualised and important quantities, such as velocity and pressure which are difficult (and expensive) to find experimentally, to be measured.

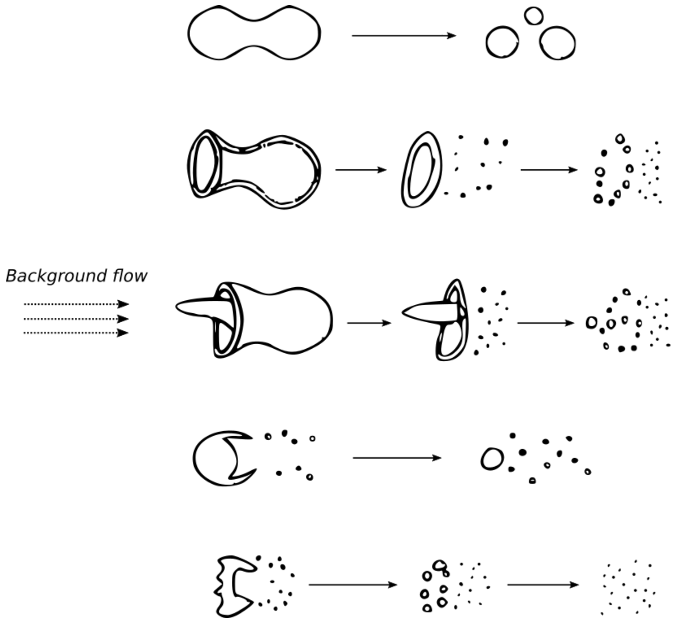

FIG. 1. From top to bottom: the vibrational, bag, multi-mode, sheet-thinning and catastrophic modes of breakup. Adapted from Guildenbecher et al.[19].

Pre-impact studies[22–24] using DNS focus primarily on identifying the different types of breakup regimes that have been observed experimentally, looking in more detail as to what processes (such as RTP and SIE) and dimensionless conditions lead to breakup. There is also a strong focus on using DNS for post-impact dynamics, helping to quantify water retention or 'blow off' from an aircraft wing following droplet impact[25]. Ideally, all aspects including the droplet, the interface, the flow field and approaching aerofoil would be investigated numerically, however such a problem is computationally infeasible with large fluid density, viscosity and length ratios posing significant numerical convergence challenges.

Motivating this report is the need for a model that accurately predicts droplet displacement, deformation and breakup in the vicinity of an approaching aerofoil. To do this, the instabilities that drive the balance of forces in the flow need to be quantified. This report considers the coupled droplet trajectory and deformation model proposed by Sor et al.[17]. The aim is to analyse and improve this model using a DNS model that solves the Navier-Stokes equations in two fluid phases. By calculating pressure and velocity profiles close to the droplet, the DNS results are used to verify or refute certain assumptions made within the existing model and improvements are subsequently suggested. It is important to determine under which flow and droplet conditions the existing model works but also when it becomes invalid (non-physical). Developing accurate predictive droplet impingement and breakup models is crucial for the aviation sector and recent advances in numerical, modelling and experimental methods should be utilised to achieve this.

The report is structured as follows. Section II outlines and examines the droplet trajectory and deformation model proposed by Sor et al[17]. Section III details the DNS model used to solve the same problem. In Section IV, results from the DNS are examined in order to suggest what could be improved in the existing model. Finally in Section V, conclusions and avenues for future investigation are drawn.

II. THE EXISTING MODEL

In this Section, an introduction to the droplet trajectory and deformation model developed by Sor et al.[17] is presented. Qualitative details of the model assumptions, background flow, droplet deformation and their coupling are given, alongside a mathematical description of the model as laid out by the authors. Minor clarifications and corrections are made to certain governing equations and an attempt is made to recreate some of the results found in the paper. Following this, the critical assumptions and limitations of the model are discussed with respect to sensitivity analysis, identifying which features are physically accurate and appropriately defined.

A. Overview and assumptions

The model tracks both the trajectory and deformation of a water droplet under the influence of an accelerating airflow. The proposed governing equations, solved numerically, are validated (and to an extent informed) using experiments carried out in a rotating arm facility[18]. Droplet motion and deformation is modelled in two dimensions[26], where an initially spherical droplet of radius r_d is placed with its centre of mass at the coordinate system origin, see Fig. 2. The incoming aerofoil approaches from the positive x direction (note that only the airflow is modelled, not the aerofoil itself), accelerating the background flow around the droplet, propelling it in the negative x and y directions. It is assumed the droplet deforms as an oblate spheroid with instantaneous semi-major and -minor axes $a(t)$ and $b(t)$ respectively. The dependent variables $x(t)$ and $y(t)$ track the droplet's centre of mass in the horizontal and vertical directions as it accelerates. No breakup of the droplet is considered in this model, hence its volume $4\pi r_d^3/3$ is conserved for all time. This means that $b(t)$ can be recovered using the spheroidal geometrical relation $r_d^3 = a^2 b$. The three time-dependent quantities of interest are therefore $x(t)$, $y(t)$ and $a(t)$. Henceforth the subscripts 1 and 2 will refer to water and air quantities respectively.

To determine the (accelerating) background air velocity profile $\boldsymbol{V}_{air} = (V_{air_x}, V_{air_y})$, a particle image velocimetry[18] system is used, experimentally modelling the aerofoil approaching droplets at constant velocity U_∞. Although no analytical formula is given, V_{air_x} is shown to exponentially increase as the aerofoil approaches the droplet. Methods for approximating this velocity profile are discussed further in later Sections.

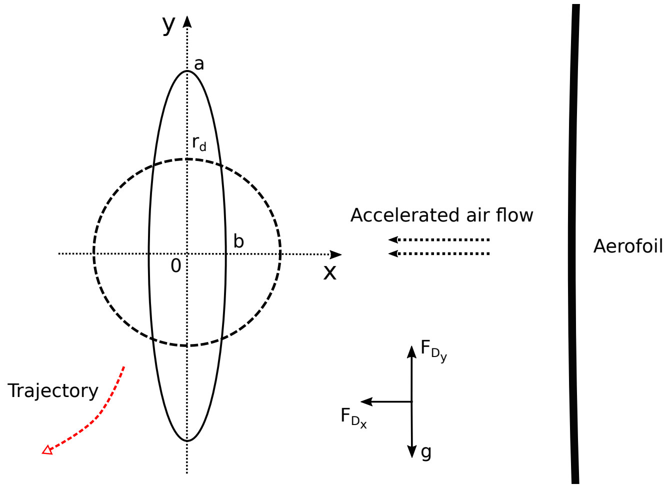

FIG. 2. Cross-sectional depiction of an oblate spheroidal droplet (solid line) with semi-major and -minor axes of length a and b respectively, having deformed from an initial spherical shape (dashed line). The incoming aerofoil (not modelled) is shown accelerating air flow in the negative x direction. Forces acting to displace the droplet are also shown.

The critical assumptions made in the model are that:

1. The vertical component of the background air velocity profile is negligible, hence $|V_{air_y}| \approx 0$.

2. The droplet deforms as an oblate spheroid, in the directions perpendicular (y and z) to the incoming flow, which, as per the first assumption, is dominated by the x component of the airflow.

3. No breakup of the droplet is considered at any point in its evolution, hence its volume is conserved.

4. The drag coefficient of the droplet is the sum of both steady and unsteady aerodynamic effects.

These assumptions were made following the completion of the experimental study. The first implies that the model is only valid close to the stagnation streamline of the incoming aerofoil, else $|V_{air_y}| > 0$. It also implies forcing terms in the deformation equation (see below) depend only on the x component of the flow. This decouples the horizontal displacement and deformation equations from the vertical displacement. As deformation is restricted to an oblate spheroidal shape, all higher order deformations on the surface of the droplet, such as those depicted in Fig. 1, are not considered. Ensuring the droplet cannot break up simplifies the dynamics drastically, thus conserving mass and shape. The final assumption incorporates the unsteady (accelerating) air flow into the drag coefficient. Further analysis of these assumptions and their implications is given in the following Sections.

B. Governing equations

The equations of motion (1a)-(1b) and deformation (1c) are stated explicitly using Newton's second law as

$$m\frac{d^2x}{dt^2} = -F_{D_x}, \tag{1a}$$

$$m\frac{d^2y}{dt^2} = F_{D_y} - mg, \tag{1b}$$

$$m\frac{d^2a}{dt^2} = F_p - F_{st} - F_v, \tag{1c}$$

where $m = 4\pi r_d^3 \rho_1/3$ is the droplet mass (ρ_1 the water density) and g the gravitational acceleration. Both F_{D_x} and F_{D_y} represent the aerodynamic drag forces acting through the droplet centre of mass in the x and y directions respectively. The three terms F_p, F_v and F_{st} represent the net pressure, viscous and surface tension forces acting on the droplet. Recall the pressure force, set up by the accelerating flow, acts on the surface to deform the droplet whereas viscosity and surface tension forces oppose it.

Using the well-known drag equation, the aerodynamic drag forces are approximated as

$$F_{D_x} \approx \frac{1}{2}\rho_2 (C_{D_1} + C_{D_2}) V_{s_x}^2 \pi a^2, \tag{2a}$$

$$F_{D_y} \approx \frac{1}{2}\rho_2 C_{D_1} V_{s_x} V_{s_y} \pi a^2, \tag{2b}$$

where ρ_2 is the air density; C_{D_1} and C_{D_2} the steady and unsteady drag coefficients; V_{s_x} and V_{s_y} the slip velocities in x and y; and πa^2 the projected area of the droplet on the plane perpendicular to the direction of the flow.

Equation (2a) is a physically valid approximation, however it is unclear why equation (2b) depends on $V_{s_x} V_{s_y}$, not $V_{s_y}^2$, as well as πa^2 instead of an ellipsoidal projected area πab (looking down on the droplet). This seemingly overestimates the vertical drag force acting on the droplet by a factor of a^3 (using the relation between a and b).

The slip velocity $\boldsymbol{V_s}$ is defined as the difference between the instantaneous velocity of the droplet and the background air velocity (recalling V_{air_y} is assumed negligible)

$$V_{s_x} = \frac{dx}{dt} - V_{air_x}, \quad V_{s_y} = -\frac{dy}{dt}. \tag{3}$$

The total drag coefficient $C_D = C_{D_1} + C_{D_2}$ is defined as the sum of steady and unsteady drag components respectively

$$C_{D_1} = C_{D_{sphere}}^{b/a} C_{D_{disk}}^{1-b/a}, \tag{4a}$$

$$C_{D_2} = \frac{kb}{V_{s_x}^2}\frac{dV_{s_x}}{dt}. \tag{4b}$$

The steady term C_{D_1} is a product of the drag coefficient of a perfect sphere and that of a flat disk (the shape of the deformed droplet perpendicular to the flow). Despite $C_{D_{disk}} = 1.17$ being a fixed constant, $C_{D_{sphere}}$ is allowed to vary with instantaneous Reynolds number: $\mathrm{Re} = \rho_2 V_{s_x} 2a/\mu_2$ (where μ_2 is the dynamic viscosity of air). This seems strange considering $C_{D_{sphere}}$ is supposed to be steady, not varying with time-dependent terms. No explicit formula is given for $C_{D_{sphere}}$ however a typical drag law[7], plotted in Fig. 3, is given as

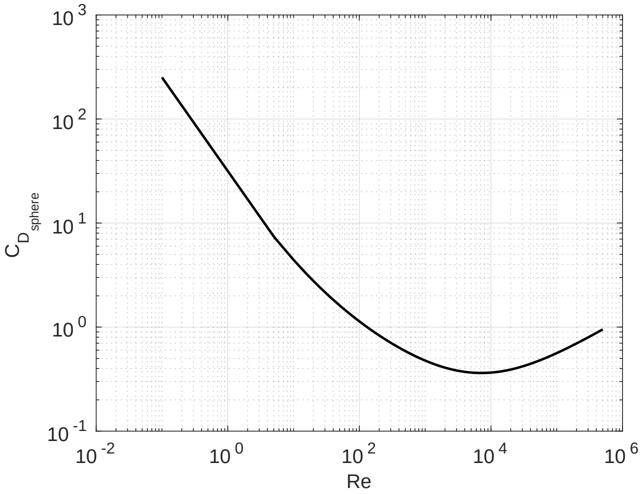

FIG. 3. The drag coefficient for a perfect sphere against varying Reynolds number, as defined by equation (5).

$$C_{D_{sphere}} = \frac{24}{\mathrm{Re}}(1 + 0.197\mathrm{Re}^{0.68} + 0.00026\mathrm{Re}^{1.38}). \tag{5}$$

The oblate spheroidal assumption implies $a \geq b$ for all time, hence the exponents in (4a) act as interpolating parameters between the two different drag coefficients ($a = b$ at $t = 0$ and $a > b$ for large t). No physical interpretation is provided for this term, with the authors stating it was used retrospectively to agree with experimental results.

The unsteady term C_{D_2} is proportional to an acceleration parameter and an experimentally calibrated coefficient $k = 9$. This term incorporates the acceleration of the flow field however the cited literature[27] only validates its use experimentally for small ($r_d \approx 115 - 187\mu m$) undeformable droplets and Reynolds numbers (9-115). These values are much smaller than those found in the experiments[17,18].

Regarding the forces in (1c), the incoming air flow sets up an imbalanced pressure distribution across the droplet, exerting a force

$$F_p = \frac{8}{3} C_p \rho_2 V_{s_x}^2 \pi r_d^2, \tag{6}$$

on its face, that acts to deform it. It is assumed proportional to the initial projected area of the droplet face πr_d^2. It is argued that pressure drops sharply away from the stagnation streamline and that using πr_d^2 instead of the instantaneous area πa^2 fits the experimental results more accurately. This approximation will be examined in Section IV when the non-uniform pressure distribution is calculated in front of the droplet. The term C_p is another experimentally calibrated pressure coefficient defined as 0.93.

Resisting pressure is the interfacial surface tension force

$$F_{st} = \frac{64}{9}\sigma\frac{dA_d}{da}, \tag{7}$$

which is proportional to the product of the surface tension of water σ and the rate of change of the droplet's surface area with respect to deformation a. The surface area of an oblate spheroid is given by

$$A_d = 2\pi a^2 + \frac{\pi b^2}{\varepsilon}\ln\left(\frac{1+\varepsilon}{1-\varepsilon}\right), \tag{8}$$

where $\varepsilon^2 = 1-(b/a)^2$ defines the eccentricity. The derivative is found by substituting in $b = r_d^3/a^2$ and differentiating to find[28]

$$\frac{dA_d}{da} = 4\pi a + \frac{6\pi r_d^6}{\varepsilon^2 a^5} - \left[\frac{3\pi r_d^{12}}{\varepsilon^3 a^{11}} + \frac{4\pi r_d^6}{\varepsilon a^5}\right]\ln\left(\frac{1+\varepsilon}{1-\varepsilon}\right). \tag{9}$$

Therefore when the droplet is spherical at $t = 0$ ($a \to 1$), there exists a minimum in the surface area ($dA_d/da \to 0$) and the tension force (7) is zero. The viscous force also opposes droplet deformation and is proportional to the energy dissipation found in two-dimensional flow

$$F_v = \frac{256}{9}m\frac{\mu_1}{\rho_1}\frac{1}{a^2}\frac{da}{dt}, \tag{10}$$

where μ_1 is the dynamic viscosity of water. This very small force is neglected in the model due to the relatively large size of the droplets under study, however its contribution will be calculated explicitly in Section II E.

C. Nondimensionalisation

With all the necessary terms in place, the equations are nondimensionalised using the following scalings

$$X = \frac{x}{r_d},\ Y = \frac{y}{r_d},\ \alpha = \frac{a}{r_d},\ \tau = \frac{tU_\infty}{r_c},$$
$$\bar{\boldsymbol{V}}_s = \frac{\boldsymbol{V}_s}{U_\infty},\ \bar{\boldsymbol{V}}_{air} = \frac{\boldsymbol{V}_{air}}{U_\infty},\ \bar{A}_d = \frac{A_d}{r_d^2},$$

where r_c is the radius of curvature of the incoming aerofoil. The dimensionless equations of motion and deformation are

$$\frac{d^2X}{d\tau^2} = \frac{\Gamma_1\Gamma_2(d\bar{V}_{air_x}/d\tau) - \Gamma_1\alpha^2\bar{V}_{s_x}^2 C_{D_{sphere}}^{\alpha^{-3}} C_{D_{disk}}^{1-\alpha^{-3}}}{1+\Gamma_1\Gamma_2^2/k}, \tag{11a}$$

$$\frac{d^2Y}{d\tau^2} = \Gamma_1\alpha^2\bar{V}_{s_x} - \Gamma_3\bar{V}_{s_y} C_{D_{sphere}}^{\alpha^{-3}} C_{D_{disk}}^{1-\alpha^{-3}}, \tag{11b}$$

$$\frac{d^2\alpha}{d\tau^2} = \Gamma_5\frac{1}{\alpha^2}\frac{d\alpha}{d\tau} - \Gamma_4\frac{d\bar{A}_d}{d\alpha} + \frac{16}{3}\Gamma_1 C_p\bar{V}_{s_x}^2, \tag{11c}$$

where the dimensionless parameters are given by

$$\Gamma_1 = \frac{3}{8}\frac{\rho_2}{\rho_1}\left(\frac{r_c}{r_d}\right)^2,\quad \Gamma_2 = k\frac{r_d}{r_c},\quad \Gamma_3 = \frac{gr_c}{U_\infty^2}\frac{r_c}{r_d},$$
$$\Gamma_4 = \frac{16}{3\pi}\frac{\sigma}{\rho_1 U_\infty^2 r_d}\left(\frac{r_c}{r_d}\right)^2,\quad \Gamma_5 = \frac{256}{9}\frac{\mu_1}{U_\infty r\rho_1}\left(\frac{r_c}{r_d}\right).$$

These equations can be solved using any suitably accurate integration method[29]. They are initialised using the following conditions

$$X(0) = 0,\quad \frac{dX}{d\tau}(0) = \frac{U_0}{U_\infty}\frac{r_c}{r_d}, \tag{12a}$$

$$Y(0) = 0,\quad \frac{dY}{d\tau}(0) = \frac{V_0}{U_\infty}\frac{r_c}{r_d}, \tag{12b}$$

$$\alpha(0) = 1,\quad \frac{d\alpha}{d\tau}(0) = 0, \tag{12c}$$

with the droplet centred at the origin with dimensionless radius equal to unity. The derivatives initialise dimensionless velocities using the corresponding dimensional initial velocities U_0 and V_0. Note that Sor et al. define $U_0 = 0$ in (12a) however their results contradict this, clearly having been initialised using a non-zero U_0 (see Section II E).

The final quantity to define is the travelling wave profile $\bar{V}_{air_x}$. Despite not being stated in the model, a future study[30] suggests using an exponential form

$$\bar{V}_{air_x}(X,\tau) = \exp\left(\tau - \frac{r_0}{r_c} + \frac{r_d}{r_c}X\right), \tag{13}$$

extrapolated from experimental results. The quantity r_0 is the initial (dimensional) distance between the droplet and the aerofoil. This is not discussed at length and will be shown to only marginally impact dynamics. Two alternative methods for defining the background flow will be discussed in Section III B.

D. Flow parameters

The dimensionless numbers (14)-(16) play an important role in quantifying the physical properties and forces that drive droplet dynamics on a wide range of scales, aiding the comparison of experimental and numerical results. The Reynolds number (14) describes the ratio of inertial to viscous forces within each fluid, with larger values indicating more turbulent flow (note $D = 2r_d$). Both are related via the density and dynamic viscosity ratios (15). The Weber number (16) is commonly used in droplet dynamic settings, describing the ratio of dynamic pressure to surface tension forces. A higher We usually signifies larger droplet deformations and more unstable breakup effects. Finally, the Froude number (16) gives the ratio of inertial to external field forces (in this case gravity). Large values indicate gravity has little effect on dynamics.

$$\mathrm{Re}_1 = \frac{\rho_1 U_\infty D}{\mu_1} \qquad \mathrm{Re}_2 = \frac{\rho_2 U_\infty D}{\mu_2} = \frac{\rho}{\mu}\mathrm{Re}_1 \tag{14}$$

$$\rho = \frac{\rho_2}{\rho_1} \qquad \mu = \frac{\mu_2}{\mu_1} \tag{15}$$

$$\mathrm{We} = \frac{\rho_1 U_\infty^2 D}{\sigma} \qquad \mathrm{Fr} = \frac{U_\infty}{\sqrt{gD}} \tag{16}$$

In order to reproduce the lab-based experimental results[16,17], physical quantities are selected at atmospheric pressure and ambient air temperature 20°C. Fixed

Case	r_d (μm)	Re$_1$	Re$_2$	We	Fr
1	287.5	52230	3463	65288	1212
2	387.5	70397	4668	87997	1044
3	512.5	93106	6174	116383	907

TABLE I. Sor et al. test cases and corresponding dimensionless numbers using $U_\infty = 91\,\mathrm{m\,s^{-1}}$.

Case	r_d (μm)	Re$_1$	Re$_2$	We	Fr
4	26	4049	268	4338	3453
5	77	11990	795	12848	2007
6	118	18375	1218	19687	1621

TABLE II. More realistic droplet sizes[31] and corresponding dimensionless numbers using $U_\infty = 78\,\mathrm{m\,s^{-1}}$.

water and air densities are stated as $\rho_1 = 998.19\,\mathrm{kg\,m^{-3}}$ and $\rho_2 = 1.20\,\mathrm{kg\,m^{-3}}$, whilst the corresponding dynamic viscosities are $\mu_1 = 1 \times 10^{-3}\mathrm{kg\,m^{-1}\,s^{-1}}$ and $\mu_2 = 1.813 \times 10^{-5}\mathrm{kg\,m^{-1}\,s^{-1}}$. The surface tension between the two fluids is $\sigma = 7.28 \times 10^{-2}\mathrm{N\,m^{-1}}$.

Ideally, real-world flight conditions[31,32] require parameters adjusted to account for aircraft altitude and temperatures close to freezing. Of interest are altitudes close to take-off and landing (i.e. when travelling through clouds) and aircraft speeds of approximately 70-90 $\mathrm{m\,s^{-1}}$ (not cruising altitude speeds). The aerofoil speeds tested by Sor et al. range from $51\,\mathrm{m\,s^{-1}}$ to $91\,\mathrm{m\,s^{-1}}$ with chord radii from 0.03 m to 0.103 m. These align well with realistic conditions however the droplet sizes tested are much larger than those typically suspended in clouds due to current imaging limitations. Table I specifies these droplet sizes alongside the corresponding dimensionless numbers at the highest aerofoil velocity. Table II details more realistic droplet sizes and quantities from Papadakis et al.[31]. The droplets in Table II are more relevant to aeronautical applications, however they are much more difficult to image experimentally.

To test the model systematically, Case 1 (corresponding to Fig. 10 in Sor et al.[17]) is chosen for analysis, using aerofoil speed $U_\infty = 91\,\mathrm{m\,s^{-1}}$ and chord radius $r_c = 0.103\,\mathrm{m}$. Although the droplet is much larger than those in clouds, it provides a good place to begin sensitivity analysis on the model.

E. Sensitivity analysis

The model requires three final inputs before it can be run, tested and analysed. The initial horizontal velocity, specified as $U_0 = 0$ in the original model, was found to actually be $U_0 = -0.865\,\mathrm{m\,s^{-1}}$ by extrapolating the derivative of the horizontal displacement at $\tau = 0$ (from Fig. 10 of the paper[17]). The initial vertical velocity was originally defined as the terminal velocity of the falling droplet but here is arbitrarily set to $V_0 = 1\,\mathrm{m\,s^{-1}}$. The Y trajectory is decoupled from both X and α, hence V_0 only affects Y. Even though small compared to U_∞, these two velocities will be shown to have a profound impact on droplet displacement and therefore must be specified carefully. The final parameter, not defined in the original model, is r_0. Being a free parameter, it is calibrated as $r_0 = 1.15 r_c$ in order to match results from Fig. 10 of the paper.

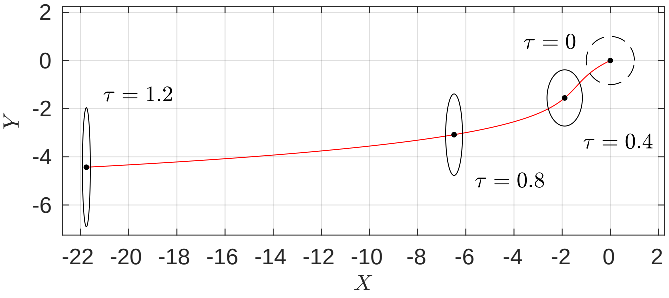

FIG. 4. Trajectory (red) and deformation (solid black) of an initially spherical droplet (dashed black) at successive dimensionless times τ in two-dimensional space.

By solving equations (11a)-(11c), together with conditions (12a)-(12c), the trajectory and deformation of the droplet over 1.2 dimensionless time units, corresponding to 1.36 ms, is plotted in Fig. 4. This time corresponds to the instant just before the aerofoil comes into contact with the droplet. As expected, the droplet is accelerated in the negative X direction by the (exponentially) increasing background air velocity, falling slightly in Y under gravity and its vertical velocity. Movement in Y is very limited as the inertial force of the background flow in X dominates gravitational and vertical acceleration. To assess certain features and assumptions of the model, parameter analysis is now carried out by isolating specific components and testing their sensitivity to various changes.

Examining equation (11b), it is found that if the gravitational acceleration g is neglected, the difference between the calculated Y trajectories is only $\mathscr{O}(10^{-2})$ (see Fig. 5). This minimal effect is a result of the characteristic length D being so small that inertial effects dominate those generated by gravity (recall the large Froude numbers in Table I). Similarly the drag force created in the Y direction is minimal due to the negligible vertical background flow, an assumption that will be tested using the numerical methods in Section III. Therefore unless a large enough initial velocity V_0 is prescribed, the displacement in Y is minimal (recall Fig. 5). Droplets suspended in clouds have little to no vertical velocity anyway so neglecting both g and V_0 is physically valid. The Y displacement is of such small order compared to the size of the aerofoil ($Y r_d / r_c \sim \mathscr{O}(10^{-3})$) that it has minimal impact on dynamics as the droplet will not deviate far from the stagnation region. Note that neglecting both parameters has no impact on the dynamics of either X or α.

Contrary to the stationary condition ($U_0 = 0\,\mathrm{m\,s^{-1}}$) stated in the original model, U_0 is almost certainly non-zero in the majority of the results reported by the authors. In Fig. 6, the X displacement of the droplet is plotted using positive, negative and zero U_0, alongside the result calculated numerically by Sor et al. Note how the extrapolated velocity $U_0 = -0.865\,\mathrm{m\,s^{-1}}$ matches the result more closely than $U_0 = 0\,\mathrm{m\,s^{-1}}$. Initialising using a positive velocity pushes

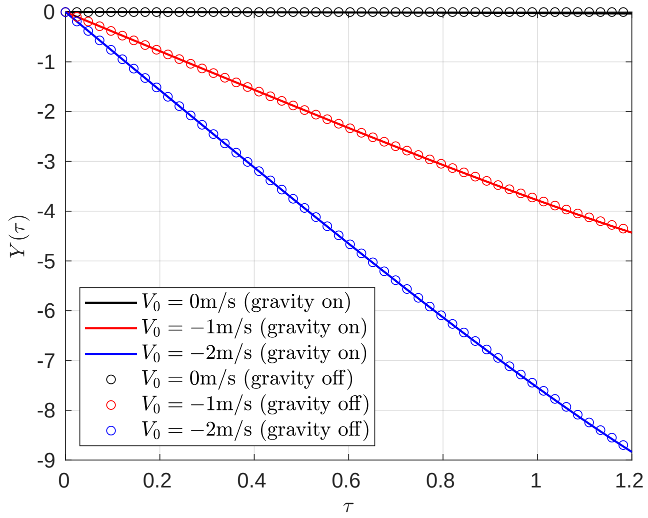

FIG. 5. The effect of varying initial vertical velocity V_0 and gravitational acceleration g on the Y trajectory of the droplet.

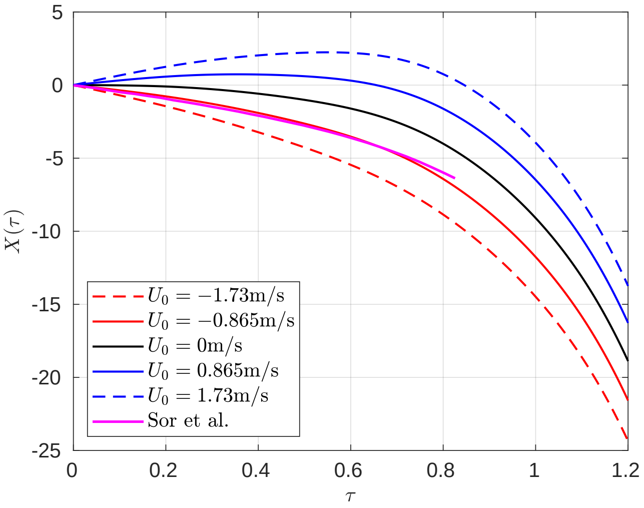

FIG. 6. The effect of varying initial horizontal velocity U_0 on the X trajectory of the droplet. Also note the corresponding Case 1 trajectory produced by Sor et al.

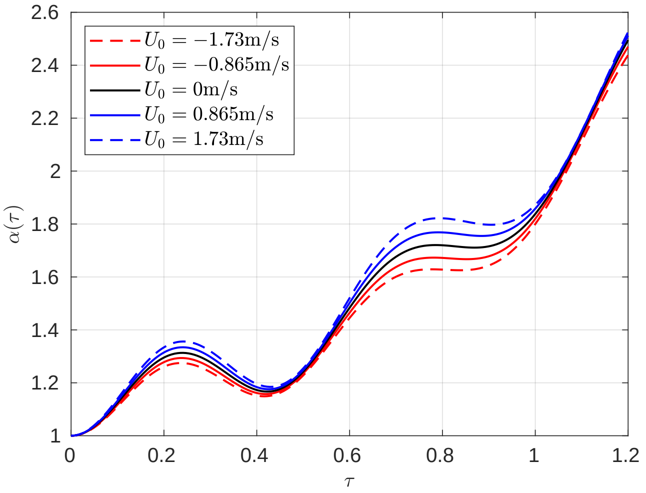

FIG. 7. The effect of varying initial horizontal velocity U_0 on the oscillatory semi-major deformation α over time.

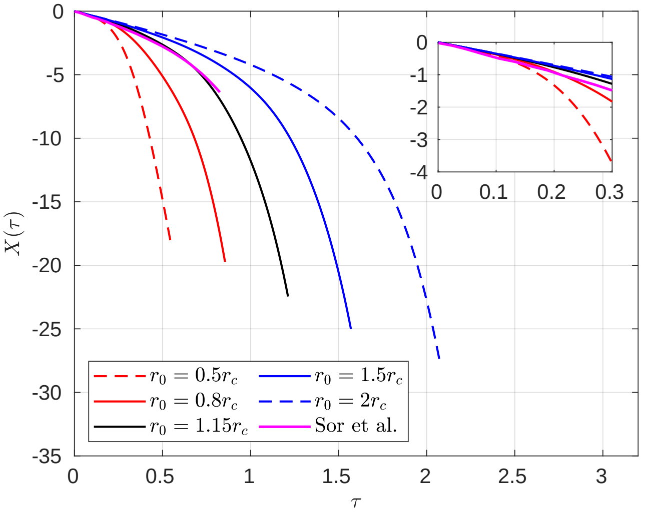

FIG. 8. Droplet displacement X against time τ for varying initial distances r_0 from the incoming aerofoil. Inset: the linear increase in X at early times τ.

the droplet towards the aerofoil, however the drag force is quickly overcome by the accelerating flow, hence the trajectory reverses direction. These varying conditions demonstrate the significant impact U_0 has on the X displacement and to a smaller, more localised, extent on α, see Fig. 7. Recall this model is built on the premise that the droplet shape oscillates over time, much like a mass-spring system, hence the semi-major axis α grows, flattening the droplet, but also oscillates on a very small scale as it does so. It is difficult to make comparisons to the original results as no plots or data on α are given.

Although temperature and altitude slightly alter the surface tension coefficient between water and air, it has minimal impact on the surface tension force. More important is the instantaneous rate of change dA_d/da in equation (7). Curiously this time-dependent quantity is used to approximate the tension, however the pressure force, which directly opposes it, is fixed proportional to an area of projection (on the droplet face) πr_d^2 instead of the true instantaneous area πa^2. This would increase the pressure force as the droplet deforms, therefore significantly increasing the deformation and trajectory of the flattened droplet. The pressure distribution will be identified more accurately in the next Section to determine whether or not this is a good approximation.

Drag forces acting on the droplet are primarily driven by changes in the slip velocity $\bar{V}_s$, which in turn is influenced by the initial position of the droplet. Increasing r_0 from $0.5r_c$ to $2r_c$ causes the droplet to feel a roughly constant background velocity (see inset of Fig. 8) for a longer period of time before accelerating with the flow. The curves end just before contact with the aerofoil and increasing r_0 above $2r_c$ has no

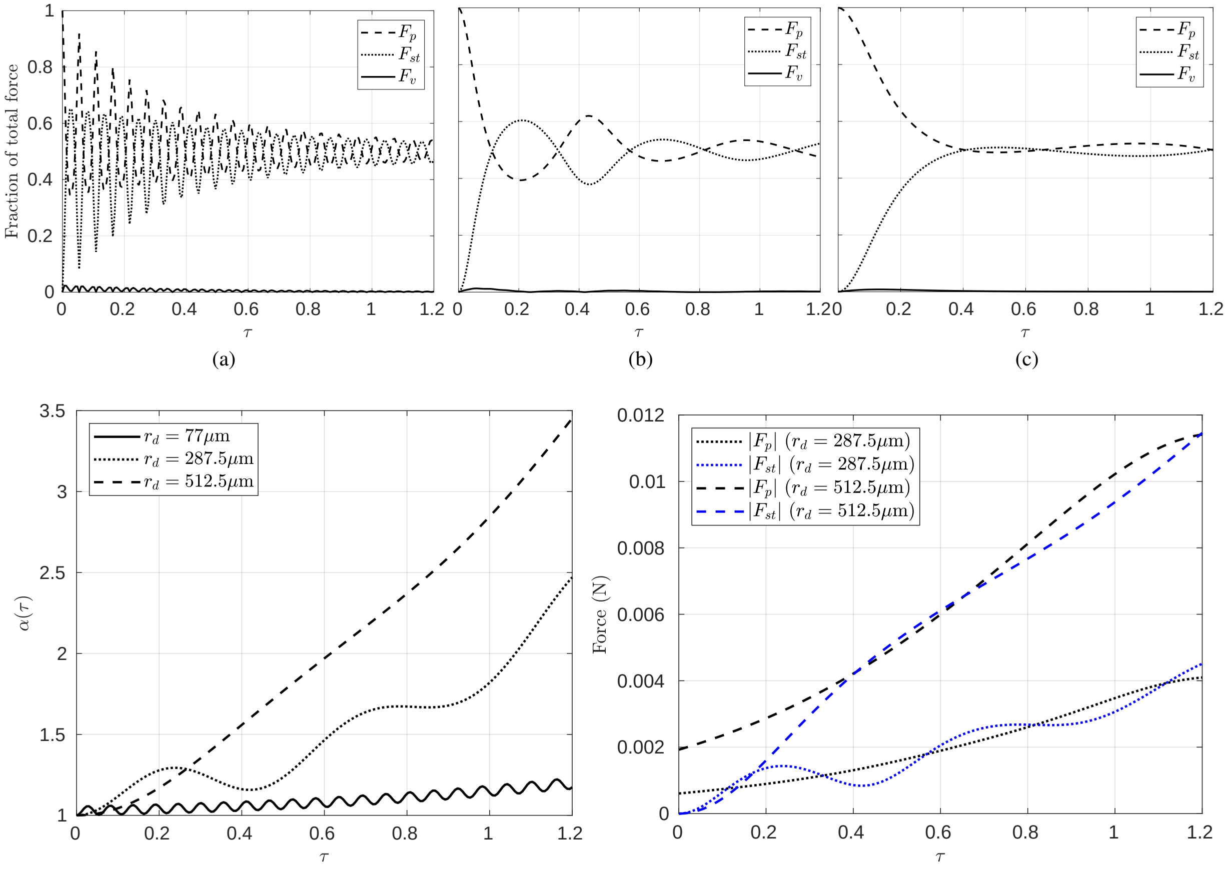

(a) (b) (c)

(d) (e)

FIG. 9. The relative magnitude of each force F_p, F_{st} and F_v acting on droplets with radius (a) $r_d = 77\mu$m, (b) $r_d = 287.5\mu$m and (c) $r_d = 512.5\mu$m, plotted as a fraction of the total force over time. (d) The corresponding deformation $\alpha(\tau)$ for each case. (e) The magnitude of the pressure and surface tension forces over time for the largest two droplets.

more effect on X as the droplet reaches maximum displacement. Thus r_0 has a minor effect on dynamics and should be set such that the droplet is initially far enough away that it feels almost none of the accelerating flow. Note that analysis on the steady and unsteady drag coefficients within the drag forces is not considered as it is out of the scope of the present report.

Figs. 9a-9c describe the fraction of the total force which pressure, surface tension and viscosity contribute to over time for varying droplet radii. Observe how the forces contest one another, causing the droplets to deform and the value of α to therefore oscillate (see Fig. 9d). Notice in each that at $\tau = 0$ the pressure force F_p, from the accelerating air flow, dominates both F_{st} and F_v. However, as the droplet begins to deform, the rate of surface area change increases and F_{st} begins to repel the deformation, continually oscillating with F_p for the rest of the simulation. Additionally, the oscillations begin to dampen over time as the velocity of the droplet approaches that of the aerofoil. Although viscosity was originally omitted from the model, it was included here to demonstrate how little impact it has compared to the other forces.

The magnitude of the forces F_p and F_{st} actually increase over time (see Fig. 9e) regardless of droplet size. This steady-state force balance is strictly a feature of the mass-spring assumption and at some time it is expected that pressure forces would overcome surface tension, leading to droplet breakup. Figs. 9c-9d show this prominently where stronger forces act on the largest droplet, deforming it rapidly and significantly with no breakup possible in the model. It is well established that at deformation levels such as this, the droplet should be undergoing some higher order deformation (into crescent-type shapes) before breaking up rapidly. Recall the sheet-thinning and catastrophic breakup modes from Fig. 1. This partly demonstrates the limitations the model has under its current assumptions.

In this Section, it has been determined that both U_0 and r_d drastically affect the balance of forces in this problem. On the other hand, the parameters g, V_0 and r_0 are much less critical to the droplet dynamics. Significant features to test using the DNS will include, for example, whether $\bar{V}_{air_y} \neq 0$ throughout the simulation. This would significantly affect the form of the drag forces in both X and Y, meaning that equations (11a)-(11c) would *all* be coupled. Viscous forces appear negligible for droplets of this size, however the approximation of the pressure force should be verified using DNS to ensure its physical validity.

The underlying assumption that droplets deform as oblate spheroids must also be considered. The initial shape deformation is clearly visible during early times of the experiments[18], yet designing a model that can capture further deformation and breakup up until the time of impact is the long term goal of interest.

Perhaps the most critical challenge of using the existing model is the reliance on parameters such as $\boldsymbol{V}_{air}$, C_p, C_D and k that require experimental data or some further intuition, guesswork or extrapolation to acquire. Using experiments to inform model assumptions is excellent for developing an accurate model that fits data and closes the governing equations, however this severely limits the reproducibility of results and hinders its predictive power. The aim of running the DNS in the next Section is to improve and/or remove such parameters and degrees of freedom in order to create a more self-contained, informative model.

III. NUMERICAL MODEL (DNS)

Firstly in this Section, the equations governing two-phase fluid motion in the droplet problem are outlined. Following this the computational domain is described, where a relatively simple but necessary simplification is made in order to speed up the numerical calculation and save computational resources. A brief description of the numerical software used to solve this problem is provided before the results are generated and analysed.

A. Mathematical formulation

Assume that both fluids 1 (water) and 2 (air) are immiscible, incompressible and viscous, retaining the same physical properties outlined in Section II D. The computational domain is a two-dimensional box with characteristic length and velocity scales D and U_∞ respectively. The nondimensional Navier-Stokes and continuity equations

$$\boldsymbol{u}_{1\bar{\tau}} + (\boldsymbol{u}_1 \cdot \nabla)\boldsymbol{u}_1 = -\nabla p_1 + \frac{1}{\mathrm{Re}_1}\nabla^2 \boldsymbol{u}_1 - \frac{1}{\mathrm{Fr}^2}\boldsymbol{F}_g, \tag{17a}$$

$$\nabla \cdot \boldsymbol{u}_1 = 0, \tag{17b}$$

$$\rho\Big(\boldsymbol{u}_{2\bar{\tau}} + (\boldsymbol{u}_2 \cdot \nabla)\boldsymbol{u}_2\Big) = -\nabla p_2 + \frac{\mu}{\mathrm{Re}_1}\nabla^2 \boldsymbol{u}_2 - \frac{\rho}{\mathrm{Fr}^2}\boldsymbol{F}_g, \tag{17c}$$

$$\nabla \cdot \boldsymbol{u}_2 = 0, \tag{17d}$$

govern the flow in each fluid and solutions must satisfy the boundary conditions, expanded on below, at the droplet interface (as well as on the box, see next Section). The equations have been nondimensionalised by scaling the lengths on D, velocities on U_∞, time on D/U_∞ and pressures on $\rho_1 U_\infty^2$. As before, due to the large Froude numbers posed by this problem, the gravity term $\boldsymbol{F}_g = (0,1)$ becomes negligible and is hence omitted. The quantities $\boldsymbol{u}_i = (u_i, v_i)$ and p_i represent the velocity vectors and pressure fields in fluid i respectively, each depending on dimensionless time $\bar{\tau}$ and space $(\bar{x}, \bar{y})$. The following coupling conditions must hold on the interface of the droplet: $\bar{y} = h(\bar{x}, \bar{\tau})$. They represent the continuity of velocity (18a); the kinematic coupling (18b); and the tangential (18c) and normal (18d) stress conditions across the interface. Note in the following that $[f_i]_2^1 = [f_1] - [f_2]$ is notation for the jump across the interface:

$$\boldsymbol{u}_1 = \boldsymbol{u}_2, \tag{18a}$$

$$v_1 = h_{\bar{\tau}} + u_1 h_{\bar{x}}, \quad v_2 = h_{\bar{\tau}} + u_2 h_{\bar{x}}, \tag{18b}$$

$$\Big[4\frac{\mu_i}{\mu} h_{\bar{x}} u_{i\bar{x}} + \frac{\mu_i}{\mu}\big(h_{\bar{x}}^2 - 1\big)\big(u_{i\bar{y}} + v_{i\bar{x}}\big)\Big]_2^1 = 0, \tag{18c}$$

$$\Big[-p_i(1+h_{\bar{x}}^2) + \frac{2}{\mathrm{Re}_1}\frac{\mu_i}{\mu}\big(h_{\bar{x}}^2 u_{i\bar{x}} + v_{i\bar{y}} - h_{\bar{x}}(u_{i\bar{y}} + v_{i\bar{x}})\big)\Big]_2^1 = \frac{1}{\mathrm{We}}\frac{h_{\bar{x}\bar{x}}^2}{\sqrt{1+h_{\bar{x}}^2}}. \tag{18d}$$

B. Computational domain

Due to the multi-phase nature of the flow and the large differences in density and viscosity between the two fluids, a robust and accurate numerical integrator is required to solve the governing equations. Simulations are carried out using the open-source code `Basilisk`[21,33], developed to solve partial differential equations on adaptive meshes. It has been demonstrated to provide second-order accurate solutions in both time and space.

To model the aerofoil, a large sphere[34] of radius r_c/D is placed at a distance r_0/D upstream of the droplet, see Fig. 10. This distance is far enough such that the droplet initially 'feels' no background air flow. It moves at velocity -1 (in the negative $\bar{x}$ direction), gradually accelerating flow around the droplet. Ideally this 'global' problem would be solved directly as stated, however attempting to compute solutions on a domain with such vast length scales (a one unit wide droplet vs. an aerofoil $2r_c/D \approx 360$ units wide) is challenging. To capture shape deformations accurately, tens of grid points are required *inside* the droplet, hence resolving over the entire domain becomes computationally infeasible and inefficient. To resolve this issue the computation is split into two parts.

The flow of interest lies close to the droplet, hence consider a much smaller 'local' computational box around it. The box spans 50 units in $\bar{x}$ and 10 in $\bar{y}$, with the droplet centre of mass initialised at $(48, 0)$. It must be both wide and high enough so that flow conditions imposed upon the boundaries do not interfere spuriously with the droplet as it evolves. An adaptive mesh, using a quadtree structure[21] is used to provide higher resolution where necessary (i.e. at the droplet interface, see Fig. 11) and lower resolution elsewhere. Grid cells have size $\mathscr{O}(2^{-\ell})$ depending on the integer level ℓ of refinement required, where $\ell \in [7, 13]$. An axisymmetric domain is used to further speed up computation, hence only a half droplet need be considered, with a symmetric boundary condition applied

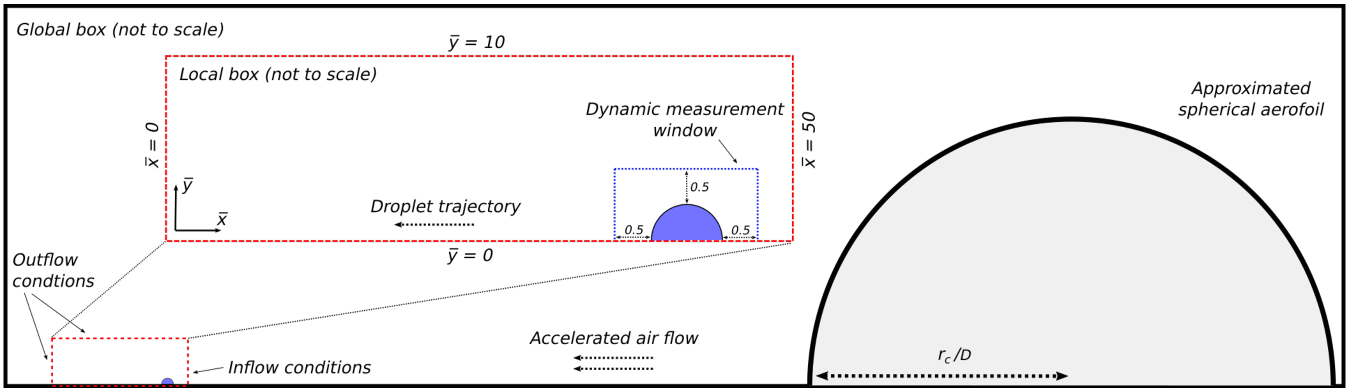

FIG. 10. Sketches of the ‘global’ and ‘local’ computational boxes used in the DNS.

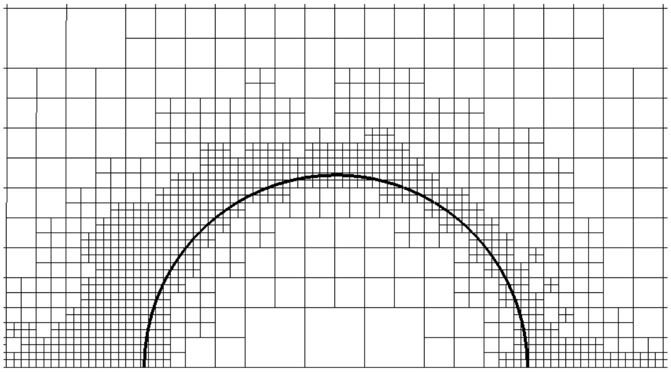

FIG. 11. The adaptive quadtree mesh used within `Basilisk`, close to the half-droplet interface. Accelerating flow is approaching from the right.

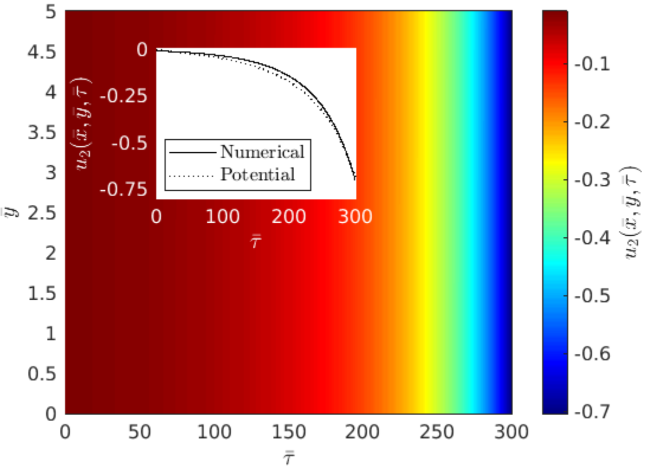

FIG. 12. Horizontal air velocity $u_2(\bar{x},\bar{y},\bar{\tau})$ computed by DNS, measured at inflow $\bar{x}=50$ over time. Inset: comparison between the DNS profile at $\bar{y}=0.5$ (the droplet top) and the corresponding analytic potential solution (A8a).

on $\bar{y}=0$. Outflow conditions are prescribed on the upper (19) and left hand boundaries (20) for all $\bar{\tau}$:

$$v_{2\bar{y}}(\bar{x},10,\bar{\tau})=0 \qquad p_2(\bar{x},10,\bar{\tau})=0 \quad \bar{x}\in[0,50], \tag{19}$$

$$u_{2\bar{x}}(0,\bar{y},\bar{\tau})=0 \qquad p_{2\bar{x}}(0,\bar{y},\bar{\tau})=0 \quad \bar{y}\in[0,10]. \tag{20}$$

These conditions enforce a continuity of flow out of the domain, imposed far enough away from the droplet as to have no effect on its dynamics. Velocity and pressure are held stationary in both fluids ($i=1,2$) at $\bar{\tau}=0$ such that

$$\boldsymbol{u}_i(\bar{x},\bar{y},0)=\boldsymbol{0} \text{ and } p_i(\bar{x},\bar{y},0)=0, \qquad (\bar{x},\bar{y})\in(0,50)\times(0,10). \tag{21}$$

By removing the droplet from the ‘global box’, simulating the moving sphere becomes a relatively computationally inexpensive task. This simulation is run, with velocity and pressure profiles being measured at the inflow boundary of the ‘local’ box ($\bar{x}=50$ between $\bar{y}=0$ and $\bar{y}=10$) over time. Analytical expressions for the profiles are then extrapolated from the resultant data and used as inflow conditions for the ‘local’ box computation.

The validity of the inflow profiles can be verified by comparing them to analytical solutions of potential flow generated in front of a sphere. The inviscid assumption of potential flow invalidates solutions close to the sphere (where boundary layers form in viscous flow). However the far-field solution, where the droplet lies, provides a good analytic approximation to the accelerating flow felt by the droplet. The velocity potential ϕ is derived in Appendix A. A comparison of the horizontal velocity inflow profile at $\bar{x}=50$ from DNS of the ‘global’ model and the analytic velocity potential is given in Fig. 12. The DNS solution for $u_2(50,\bar{y},\bar{\tau})$ matches the analytical solution (A8a) exceptionally well, with slight deviations possibly due to the inviscid nature of potential flow and numerical round-off. Similar profiles are generated for $v_2(50,\bar{y},\bar{\tau})$ and $p_2(50,\bar{y},\bar{\tau})$, closely aligning with the analytical solutions in Appendix A. Both methods therefore provide a much more robust way of calculating the accelerating velocity and pressure profiles generated by the aerofoil without having to experimentally extrapolate data as in Section II C.

IV. NUMERICAL RESULTS

To test the assumptions made in Section II, the (DNS) droplet model is solved in the 'local' computational box. To identify important flow quantities near the droplet, measurements are taken on the boundary of a dynamically moving window, much like the one used to measure the inflow conditions in the 'global' domain. Each boundary is situated one droplet radii (0.5 units) in front, behind and above the half-droplet, referring to Fig. 10.

The $\bar{x}$ displacement and maximum (vertical) deformation of the half-droplet are plotted in Fig. 13. As expected, the initially stationary half-droplet gradually gradually accelerates as the air inflow speed increases, thus propelling it across the domain and subsequently deforming it. It does not travel as quickly as in the existing model (only reaching 7% of the aerofoil speed vs. almost 18% at dimensional time $t = 1.36$ms), partly because the the maximum deformation is not as large, thus reducing the area for air to push the droplet. The deformation curve in Fig. 13 does not exhibit, at this relatively high resolution, any small scale oscillations, calling into the question the validity of the overall mass-spring approximation used in the previous droplet models in this particular parameter regime.

High resolution snapshots of the deforming interface, at later times, are given in Fig. 14. Whilst the droplet initially ($\bar{\tau} \approx 250$) deforms into a slightly oblate spheroidal shape, it becomes increasingly more squashed on its face than rear. This occurs as a result of faster (horizontal) air flow hitting the droplet face, while slower air moves behind, setting up an imbalanced pressure gradient across the droplet (see Fig. 15). This gradient grows as the droplet is accelerated. The fastest flow can be observed toward the top of the droplet ($\bar{y} \approx 0.5$), compared to the sower flow at the base (the stagnation streamline $\bar{y} = 0$). The pressure force drives the flattening process (Fig. 14c), pulling the droplet's centre of mass toward the face and leaving the interface behind more spheroidal. This is the work of the currently unknown surface tension force. At these late time stages (see Fig. 14d), the assumption of droplet spheroidicity begins to break down, as expected from previous studies of droplet deformation and breakup.

The assumption that $V_{air_y} \approx 0$ in the Sor et al. model can be validated by observing the vertical velocity of the air above the half-droplet. Fig. 16a plots the velocity profiles over $\bar{x}$, indicating where the centre of mass lies as the droplet accelerates. Fig. 16b depicts the vertical velocity field more qualitatively, with air travelling up the face and down the back of the droplet as it moves. The zero flow approximation (dashed red in Fig. 16a) is made through the centre of mass in the existing model and although values from the DNS (black dots) indicate slightly positive vertical flow above the centre of mass, the scale is $\mathscr{O}(10^{-3})$, demonstrating the flow is minimal and the assumption holds. This is valid for droplets moving parallel to the stagnation streamline, not however for droplets approaching the aerofoil at different angles.

Finally, observe the pressure field around the droplet in Fig. 17a. As expected the flow sets up higher pressure in front of the droplet, while the re-circulation region (not shown) with slower flow behind the droplet, exhibits a lower pressure. Coupled with opposing pressures inside the droplet, these act to deform the droplet as previously described. Equation (6) approximates pressure at the droplet front, assuming it "decreases sharply up from the droplet stagnation streamline region down to the droplet edge", however Fig. 17b shows pressure *increasing* sharply from the stagnation streamline to the droplet top. Pressure applies relatively uniformly across toward the droplet top, especially at earlier times, suggesting that (6) should account for the growing area πa^2 instead of the fixed πr_d^2. This strong effect plays a critical role in the non-uniform (hence non-spheroidal) deformation observed in Fig. 14d.

It should be noted that results produced here were done so with limited computational resources and time. Much more

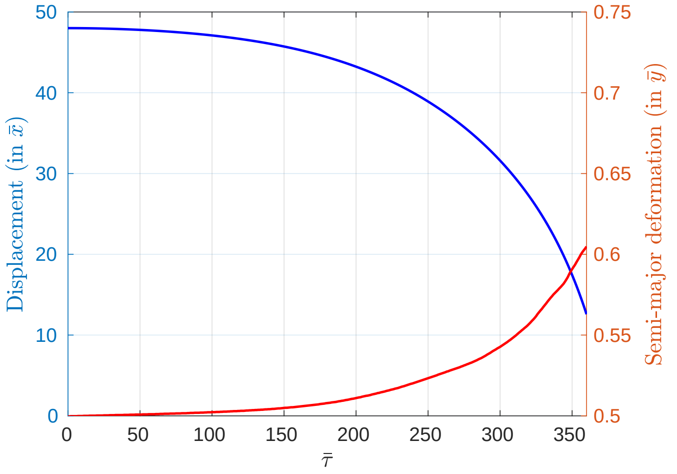

FIG. 13. Left axis: displacement of the half-droplet in $\bar{x}$ against $\bar{\tau}$. Right axis: the maximum semi-major deformation of the interface in the $\bar{y}$ direction against $\bar{\tau}$.

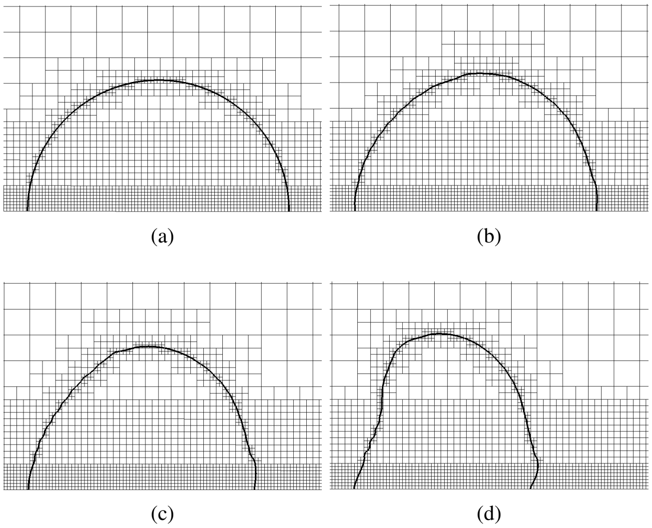
(a) (b) (c) (d)

FIG. 14. The half-droplet interface at dimensionless times (a) $\bar{\tau} = 0$, (b) $\bar{\tau} = 250$, (c) $\bar{\tau} = 300$ and (d) $\bar{\tau} = 350$.

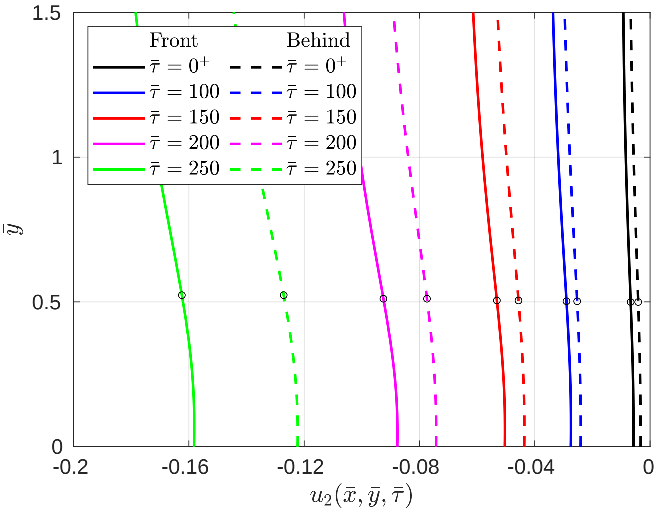

FIG. 15. Horizontal velocity profiles $u_2(\bar{x}, \bar{y}, \bar{\tau})$ against $\bar{y}$ at increasing times $\bar{\tau}$ both in front and behind the half-droplet. Black dots indicate the maximum height of the droplet interface at the corresponding $\bar{\tau}$.

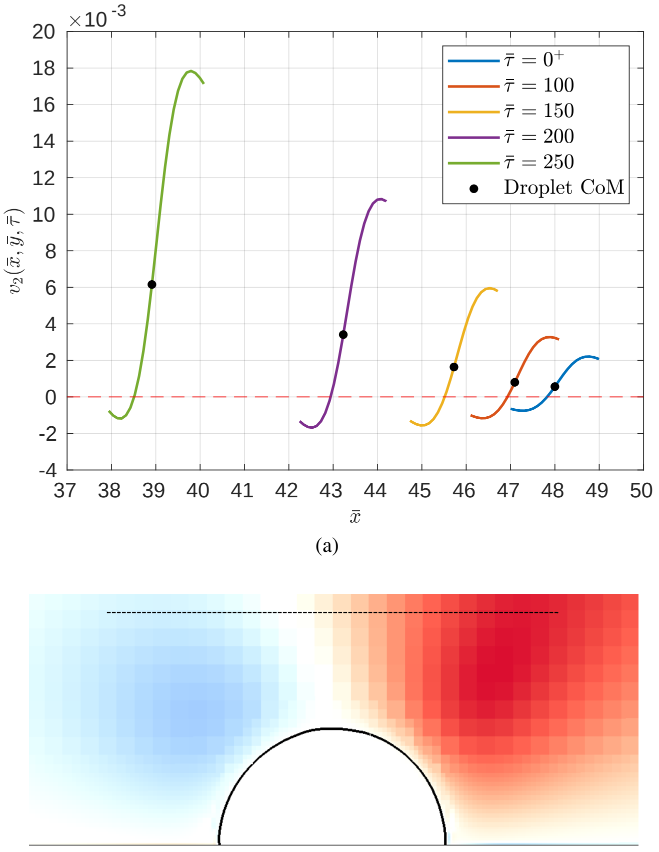

(a)

(b)

FIG. 16. (a) Vertical velocity profiles $v_2(\bar{x}, \bar{y}, \bar{\tau})$ against $\bar{x}$, above the half-droplet, at increasing $\bar{\tau}$. The half-droplet centre of mass is indicated by the black dots and the dashed red line is the zero flow assumption. (b) Vertical velocity field around the half-droplet at $\bar{\tau} = 150$. Flow speeds range from 0.006 (dark red) to 0 (white) to -0.006 (dark blue). The dashed black line indicates where the profiles in (a) were measured.

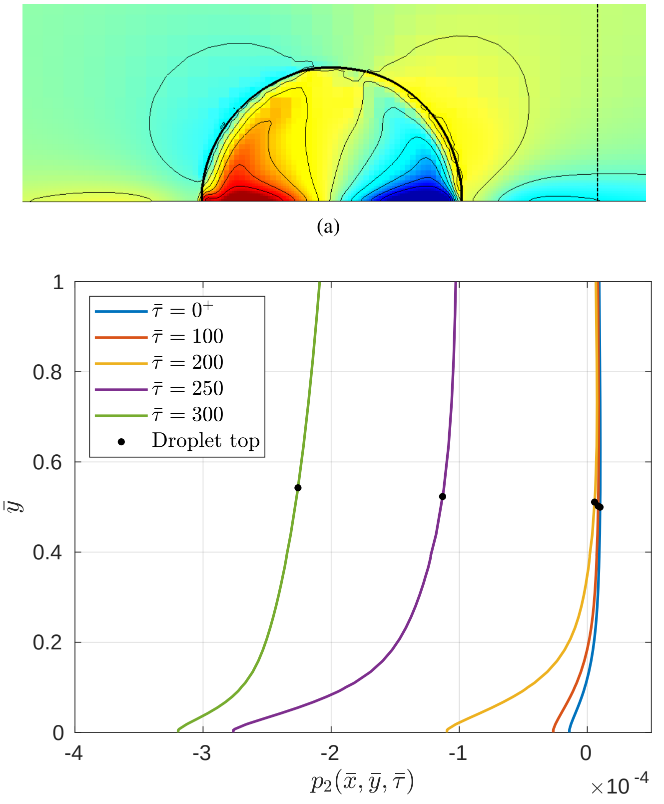

(a)

(b)

FIG. 17. (a) Pressure field inside and around the half-droplet at $\bar{\tau} = 150$. Values range from 0.0002 (dark red) to 0 (green/yellow) to -0.0002 (dark blue) with 10 evenly spaced contours between. Dashed black line indicates where profiles in (b) were taken. (b) The non-uniform pressure distribution $p_2(\bar{x}, \bar{y}, \bar{\tau})$ against $\bar{y}$, in front of the half-droplet, at increasing times $\bar{\tau}$. The top of the half-droplet is indicated by the black dots.

detailed analysis needs to be carried out, as irregularities simulating the flow close to the interface remain and need to be fully verified at multiple spatial resolutions. Even though these quantitative results are not fully numerically accurate, it was still possible to explore qualitative aspects of the flow around the half-droplet and provide an insight into the assumptions made in the existing analytical model.

V. CONCLUSIONS

In this report, a detailed analysis of an existing droplet deformation and trajectory model has been presented, evaluating critical assumptions and approximations using the highly accurate and computationally efficient DNS of decoupled droplet and aerofoil models. These assumptions consisted of using the Taylor analogy, no vertical background air flow, deformation into an oblate spheroidal shape, no breakup and unsteady drag effects among others.

The vertical flow above the deforming droplet determined that the assumption $|V_{air_y}| \approx 0$ is valid if the droplet remains in the stagnation region of the aerofoil. For small droplets suspended in clouds, both gravitational acceleration and initial vertical velocity can also be omitted from deformation and trajectory analysis. Consequently, in this stagnation region both features were omitted from the DNS as they have no impact on horizontal displacement and deformation. The droplet radii and its initial horizontal velocity did however significantly impact dynamics. Two aspects not explored, were modes of droplet breakup and the steady and unsteady drag coefficients used in the existing model. Breakup is something to be dealt with once the deformation model is better understood and, although unclear why certain assumptions were made about the drag coefficients, these quantities are not yet (in the unsteady case) fully understood for accelerating flows.

The numerically generated ('global' model) or analytical (potential flow) velocity and pressure profiles provided a much more efficient and robust way of calculating the accelerating background flow rather than extrapolating from experimental results. The DNS also showed, in this specific case, that the oblate spheroidal assumption only holds for a very short time after acceleration, after which the droplet face becomes dramatically more squashed than the its back due to flow and pressure gradients. No oscillations of the semi-major deformation were observed at this scale either. Further numerical test cases would reveal whether it is a true physical feature or just a consequence of the Taylor analogy assumption. The non-uniform pressure distribution was found to increase sharply away from the stagnation streamline, driving the interfacial shape deformation with more precision than the approximated pressure used in the existing model.

The purpose of this report was to identify the features and assumptions of the existing analytical model that were physically valid and to what extent the model could be pushed before breaking down (i.e. for large droplets $\sim$ 1mm in diameter). To do this, a self-contained droplet model, that captures all of the relevant physics associated with an accelerating airflow, was developed - something not studied previously in numerical detail.

Although not fully mature, efficiently coupling the 'local' and 'global' DNS domains was a good first attempt at reducing the computational requirements of such a detailed model. It illustrates the future potential of building a more global predictive model for studying droplet morphology in (almost) real-world flight conditions. This is an extremely challenging numerical regime that has yet to be extensively explored. Vast differences between the fluid densities and viscosities as well as high spatial resolutions on the droplet interface require significantly more computational resources the larger the droplet and domain become.

Further work is needed to fully complete and refine the DNS model. One aspect is to make the `Basilisk` code as efficient as possible, simulating flow solutions with high accuracy only where strictly necessary in the domain. By simulating in a larger 'local' box, deformation and breakup behaviour can be captured over much longer timescales. The numerical validity of results must also be investigated by solving the problem at different spatial resolutions, allowing for a much more accurate quantitative analysis that can replace some of the more limited qualitative descriptions given in this report. To study dynamics on shorter (computational) timescales, larger droplets can be considered however this moves away from the small droplets in clouds that are of real-world significance. Once the a fully functioning and efficient DNS model is up and running, an interesting avenue to explore would be to relax the $V_{air_y} \approx 0$ assumption, thereby modelling what happens to droplets above or below the stagnation region of the aerofoil. Closely following this, and computationally heavier still, would be to investigate droplet breakup modes under an accelerating flow, something only investigated for constant background flows in the literature. Coupling such a model with post-impact droplet models is something to look toward in the future as well.

The existing model represents the current state-of-the-art in modelling droplet dynamics analytically, approximating the experimental results from this highly challenging regime reasonably well. However, further analytical progress, such as attempting to relax the spheroidal assumption or including breakup, seems at present a difficult challenge. The recent advances in DNS for multi-phase flows illustrate the potential for capturing droplet dynamics at high levels of quantitative detail in these challenging regimes and the present study represents a first systematic incursion in this direction.

ACKNOWLEDGMENTS

Firstly I would like to thank my supervisors Dr. Radu Cimpeanu and Dr. Ed Brambley for their excellent help and feedback throughout this project, as well as for introducing me to the fascinating field of droplet dynamics. I would also like to thank the MathSys team for their continued support throughout these uncertain times and also the funding provided by EPSRC.

Appendix A: Potential flow around a sphere

To determine the potential flow around a sphere centred at the origin, take a spherical coordinate system with radial length r, polar angle θ and azimuthal angle γ. The problem is axisymmetric in two dimensions hence independent of γ. To determine both the velocity $\boldsymbol{u}_2 = \nabla\phi$ and the (Bernoulli) pressure field $p_2 = p_0 - \rho_2|\nabla\phi|^2/2$ around the sphere, Laplace's equation (A1) must be solved for the potential $\phi(r,\theta)$ (where p_0 is the ambient pressure). Boundary conditions include zero flow in the far field (A2a) and normal flow equal to that of the aerofoil on the circular boundary r_c (A2b).

$$\nabla^2\phi = 0 \quad \text{for} \quad r \geq r_c \tag{A1}$$

$$\nabla\phi \to 0 \quad \text{as} \quad r \to \infty \tag{A2a}$$

$$\nabla\phi \cdot \hat{\boldsymbol{n}} = -U_\infty \cos(\theta) \quad \text{on} \quad r = r_c \tag{A2b}$$

Using a separable solution of the form $\phi(r,\theta) = R(r)T(\theta)$, equation (A1) can be written as two inhomogeneous second-order differential equations (A3a)-(A3b), dependent upon a common eigenvalue λ.

$$r^2 R_{rr} + 2rR_r - \lambda R = 0, \tag{A3a}$$

$$\big(\sin(\theta) T_\theta\big)_\theta + \lambda \sin(\theta) T = 0. \tag{A3b}$$

Take a solution of the form $R_n(r) = A_n r^n + B_n r^{-(n+1)}$ with constants A_n and B_n for $n \in \mathbb{N}_0$. Substituting into (A3a) this yields eigenvalues of the form $\lambda_n = n(n+1)$. Next take $\theta = \arccos(x)$ and transform equation (A3b) into

$$\big((1-x^2)T_x\big)_x + n(n+1)T = 0, \tag{A4}$$

which is Legendre's differential equation. Solutions take the form $T_n(x) = P_n(x) = P_n(cos(\theta))$ where P_n are the complete, orthogonal Legendre polynomials. The superposed solution for the potential ϕ can thus be written as

$$\phi(r,\theta) = \sum_{n=0}^{\infty} \Big(A_n r^n + B_n r^{-(n+1)}\Big) P_n(\cos(\theta)). \tag{A5}$$

Boundary condition (A2a) implies solutions must decay, hence $A_n = 0 \; \forall n \in \mathbb{N}$ whilst (A2b) implies the normal derivative

$$\phi_r = -\sum_{n=0}^{\infty} (n+1) B_n r^{-(n+2)} P_n(\cos(\theta)) = -U_\infty \cos(\theta), \tag{A6}$$

at $r = r_c$. Comparing coefficients, the only Legendre polynomial of the form $\cos(\theta)$ is P_1, hence the only non-zero constant is $B_1 = U_\infty r_c^3/2$. The final solution is therefore

$$\phi(r,\theta) = \frac{U_\infty}{2} \frac{r_c^3}{r^2} \cos(\theta) \quad \text{for} \quad r \geq r_c. \tag{A7}$$

The DNS simulations require dimensionless profiles, hence the flow components and pressure field are found (in Cartesian form) to be

$$u_2(\bar{x},\bar{y}) = -\left(\frac{r_c}{D}\right)^3 \frac{\bar{x}}{(\bar{x}^2+\bar{y}^2)^2}, \tag{A8a}$$

$$v_2(\bar{x},\bar{y}) = \frac{1}{2}\left(\frac{r_c}{D}\right)^3 \frac{\bar{y}}{(\bar{x}^2+\bar{y}^2)^2}, \tag{A8b}$$

$$p_2(\bar{x},\bar{y}) = \bar{p}_0 - \frac{\rho}{8}\left(\frac{r_c}{D}\right)^6 \frac{(4\bar{x}^2+\bar{y}^2)}{(\bar{x}^2+\bar{y}^2)^4}, \tag{A8c}$$

for $\bar{x}^2 + \bar{y}^2 \geq (r_c/D)^2$. Note that these profiles must be shifted in $\bar{x}$ according to where the sphere is placed in the flow domain (i.e. r_0/D units away from the origin).

[1] M. M. Mohebi and J. R. Evans, "The trajectory of ink-jet droplets: Modelling and experiment," Chemical Engineering Science **60**, 3469–3476 (2005).

[2] M. A. Delele, D. Nuyttens, A. T. Duga, A. Ambaw, F. Lebeau, B. M. Nicolai, and P. Verboven, "Predicting the dynamic impact behaviour of spray droplets on flat plant surfaces," Soft Matter **12**, 7195–7211 (2016).

[3] D. Attinger, C. Moore, A. Donaldson, A. Jafari, and H. A. Stone, "Fluid dynamics topics in bloodstain pattern analysis: Comparative review and research opportunities," Forensic Science International **231**, 375–396 (2013).

[4] T. Dbouk and D. Drikakis, "On coughing and airborne droplet transmission to humans," Physics of Fluids **32**, 53310 (2020).

[5] F. Caliskan and C. Hajiyev, "A review of in-flight detection and identification of aircraft icing and reconfigurable control," Progress in Aerospace Sciences **60**, 12–34 (2013).

[6] Y. Cao, Z. Wu, and Z. Xu, "Effects of rainfall on aircraft aerodynamics," Progress in Aerospace Sciences **71**, 85–127 (2014).

[7] R. W. Gent, N. P. Dart, and J. T. Cansdale, "Aircraft icing," Philosophical Transactions of the Royal Society A: Mathematical, Physical and Engineering Sciences **358**, 2873–2911 (2000).

[8] A. Yarin, "Drop Impact Dynamics: Splashing, Spreading, Receding, Bouncing…," Annual Review of Fluid Mechanics **38**, 159–192 (2006).

[9] C. Josserand and S. Thoroddsen, "Drop Impact on a Solid Surface," Annual Review of Fluid Mechanics **48**, 365–391 (2016).

[10] One of the few investigations in this area uses second-order asymptotic methods to predict the deformation and breakup of an inviscid droplet for varying dimensionless numbers[35].

[11] P. O'Rourke and A. Amsden, "The TAB method for numerical calculation of spray droplet breakup," SAE Paper (1987).

[12] G. Taylor, "The shape and acceleration of a drop in a high-speed air stream," in *The Scientific Papers of Sir Geoffrey Ingram Taylor*, edited by G. Batchelor (Cambridge University Press, 1963) 3rd ed.

[13] M. Clark, "Drop breakup in a turbulent flow-I. Conceptual and modeling considerations," Chemical Engineering Science **43**, 671–679 (1988).

[14] E. A. Ibrahim, H. Q. Yang, and A. J. Przekwas, "Modeling of spray droplets deformation and breakup," Journal of Propulsion and Power **9**, 651–654 (1993).

[15] S. A. Krzeczkowski, "Measurement of liquid droplet disintegration mechanisms," International Journal of Multiphase Flow **6**, 227–239 (1980).

[16] S. Sor and A. Garcia-Magarino, "Modeling of droplet deformation near the leading edge of an airfoil," Journal of Aircraft **52**, 1838–1846 (2015).

[17] S. Sor, A. García-Magariño, and A. Velazquez, "Model to predict water droplet trajectories in the flow past an airfoil," Aerospace Science and Technology **58**, 26–35 (2016).

[18] A. García-Magariño, S. Sor, and A. Velazquez, "Experimental characterization of water droplet deformation and breakup in the vicinity of a moving airfoil," Aerospace Science and Technology **45**, 490–500 (2015).

[19] D. R. Guildenbecher, C. López-Rivera, and P. E. Sojka, "Secondary atomization," Experiments in Fluids **46**, 371–402 (2009).

[20] T. Theofanous, "Aerobreakup of Newtonian and Viscoelastic Liquids," Annual Review of Fluid Mechanics **43**, 661–690 (2011).

[21] S. Popinet, "An accurate adaptive solver for surface-tension-driven interfacial flows," Journal of Computational Physics **228**, 5838–5866 (2009).

[22] M. Jalaal and K. Mehravaran, "Fragmentation of falling liquid droplets in bag breakup mode," International Journal of Multiphase Flow **47**, 115–132 (2012).

[23] M. Jalaal and K. Mehravaran, "Transient growth of droplet instabilities in a stream," Physics of Fluids **26**, 012101 (2014).

[24] T. Kékesi, G. Amberg, and L. Prahl Wittberg, "Drop deformation and breakup," International Journal of Multiphase Flow **66**, 1–10 (2014).

[25] R. Cimpeanu and D. T. Papageorgiou, "Three-dimensional high speed drop impact onto solid surfaces at arbitrary angles," International Journal of Multiphase Flow **107**, 192–207 (2018).

[26] Note there is no motion in the z dimension, in which the droplet also has semi-major length $a(t)$, hence it need not be modelled.

[27] S. Temkin and H. K. Mehtaf, "Droplet drag in an accelerating and decelerating flow," Journal of Fluid Mechanics **116**, 297–313 (1982).

[28] Note there is a typographical error of the corresponding derivative in equation (11) of the original model[16] which has been corrected in (9).

[29] It must be noted that the original formulation[17] of (11a) contained an acceleration term $d^2X/d\tau^2$ on its right hand side, causing confusion when integrating, hence it has been incorporated into the left hand side here.

[30] S. Sor, A. Garcia-Magariño, and A. Velazquez, "A Study of Droplet Breakup in the Vicinity of an Airfoil," in *SAE Technical Papers*, Vol. 2019-June (SAE International, 2019).

[31] M. Papadakis, A. Rachman, S. C. Wong, H. W. Yeong, K. Hung, and C. S. Bidwell, "Water impingement experiments on a NACA 23012 airfoil with

simulated glaze ice shapes," in *AIAA Paper* (2004) pp. 5528–5568.

[32] M. Hess, P. Koepke, and I. Schult, "Optical Properties of Aerosols and Clouds: The Software Package OPAC," Bulletin of the American Meteorological Society **79**, 831–844 (1998).

[33] S. Popinet, "Basilisk flow solver and library," http://www.basilisk.fr/.

[34] A cylinder would also be an appropriate geometry however a sphere was chosen to align with functionality in `Basilisk`.

[35] E. Y. Harper, G. W. Grube, and I. D. Chang, "On the breakup of accelerating liquid drops," Journal of Fluid Mechanics **52**, 565–591 (1972).